Protease-targeting peptide-functionalized porous silicon nanoparticles for cancer fluorescence imaging

Jayasree S Kanathasan[1], Uma Devi Palanisamy[2] ID, Ammu K Radhakrishnan[2] ID, Srikumar Chakravarthi[3], Tan Boon Thong[1] ID & Varghese Swamy*,[1] ID

[1]Mechanical Engineering Discipline, School of Engineering, Monash University Malaysia, Bandar Sunway, Subang Jaya, Selangor, 47500, Malaysia
[2]Jeffrey Cheah School of Medicine & Health Sciences, Monash University Malaysia, Bandar Sunway, Subang Jaya, Selangor, 47500, Malaysia
[3]MAHSA University, Jalan SP 2, Bandar Saujana Putra, Jenjarom, Selangor, 42610, Malaysia
*Author for correspondence: Tel.: +61490352981/61385020303; Varghese.swamy@monash.edu

Background: Porous silicon (pSi) nanoparticles (NPs) functionalized with suitable targeting ligands are now established cancer bioimaging agents and drug-delivery platforms. With growing interest in peptides as tumor-targeting ligands, much work has focused on the use of various peptides in combination with pSi NPs for cancer theranostics. Here, the authors investigated the targeting potential of pSi NPs functionalized with two types of peptide, a linear 10-mer peptide and its branched (Y-shaped) equivalent, that respond to legumain activity in tumor cells. **Results:** *In vitro* experiments established that the linear peptide-pSi NP conjugate had better aqueous stability under tumor conditions and higher binding efficiency (p < 0.001) toward legumain-expressing cells such as RAW 264.7 cells compared with that of its branched equivalent. *In vivo* studies (analyzed using *ex vivo* fluorescence) with the linear peptide-pSi NP formulation using a syngeneic mouse model of breast cancer showed a higher accumulation (p > 0.05) of linear peptide-conjugated pSi NPs in the tumor site within 4 h compared with nonconjugated pSi NPs. These results suggest that the linear peptide-pSi NP formulation is a nontoxic, stable and efficient fluorescence bioimaging agent and potential drug-delivery platform.

Graphical abstract:
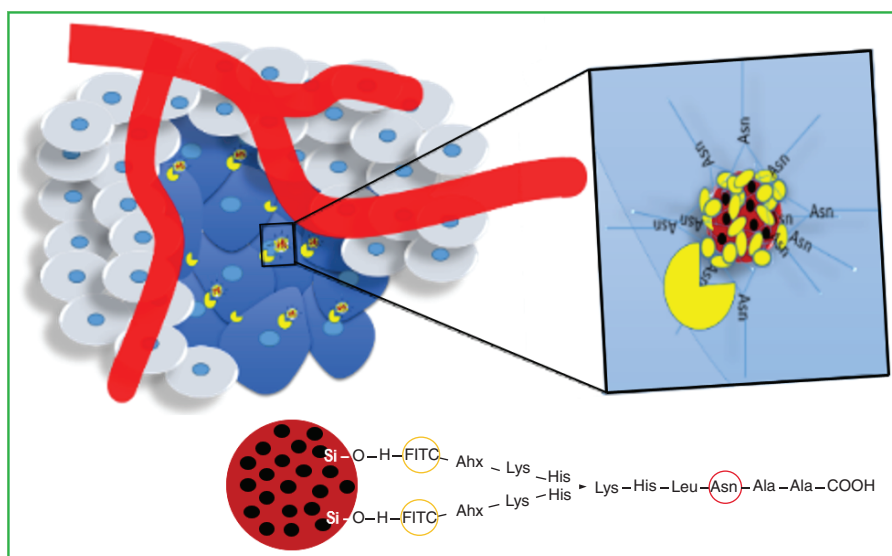
Two types of legumain-targeting peptide (linear and Y-branched) functionalized porous silicon (pSi) nanoparticles were successfully synthesized. The targeting specificity of the peptide-pSi nanoparticles toward cell-based legumain activity was established and the better performing nanoplatform was successfully tested for its bioimaging potential through *ex vivo* fluorescence imaging of extracted organs.

Cancer nanotechnology [1] has been promising innovative solutions that can overcome some of the challenges associated with conventional theranostic approaches, which include reduced specificity to tumor cells leading to treatment modalities invading healthy cells/tissues in addition to cancerous ones and resultant side effects [2]. In this context, porous silicon (pSi) nanoparticles (NPs) have attracted much attention as bioimaging and drug-delivery agents since the recognition of their intrinsic luminescence and biocompatibility in the 1990s [3,4]. Not only are pSi NPs made of an earth-abundant material, but they are also nontoxic and completely biodegradable to silicic acid (SiO_4H_4) within a short time, a trace substance in humans that can be systemically bioeliminated through renal clearance [5]. Furthermore, their particle size, pore size and highly stable photoluminescence (PL) are tunable [6], allowing drug loading and bioimaging in the near-infrared (NIR) blue emission regions [7], and the large specific surface area of pSi NPs facilitates functionalization with a range of molecules via methods such as PEGylation, hydrosilylation, silanization and hydrocarbonization as well as bioconjugation [8,9]. These attributes make pSi NPs a near-perfect candidate for multifunctional nanomedical and biosensing applications [8–11].

An early detailed study of the biodistribution, theranostic potential, biodegradation and bioelimination of ~126 nm pSi NPs produced through electrochemical etching demonstrated the excellent NIR PL and anticancer drug-carrying capabilities of the NPs and their *in vivo* biodegradation into nontoxic substances that were excreted renally within 4 weeks [5]. Several studies have appeared in the literature since then that focus on the production, surface treatments, functionalization and *in vivo* uptake of pSi NPs for bioapplications [12,13]. Of particular interest here are the various efforts aimed at effective targeting of the pSi NPs and their payloads to desired sites or tissue aided by specific functionalization and attached homing ligands. Suitable surface functionalization and ligand conjugation facilitate increased circulation of NP formulations in body fluids, especially by avoiding significant opsonization by the mononuclear phagocyte system (MPS) and increasing the probability of NP attachment at desired sites to perform the intended theranostic task [11,14]. pSi NPs have been surface-functionalized using coatings such as dextran [5], serum albumin [15] and polyethylene glycol [16] as well as with a range of tumor-targeting ligands including carbohydrates, antibodies and peptides [17–22]. Among the ligands, peptides, which possess several attractive targeting attributes [23], have recently been widely researched in conjunction with pSi NPs and other NPs for bioimaging and drug-delivery applications [18,20,23–27].

The present study focuses on targeting breast cancer cells using legumain-responsive peptide-functionalized pSi NPs with the primary aim of imaging breast tumors. Legumain, an asparaginyl endopeptidase, is a lysosomal enzyme belonging to the C13 protease family [28]. Legumain has been implicated in various pathophysiological processes. Increased levels of legumain in plasma and plaques from patients with carotid atherosclerosis as well as impacts of upregulated legumain in patients during acute cardiovascular events have been reported [29]. Legumain plays significant roles in diseases such as multiple sclerosis and Alzheimer's disease [28]. Importantly, in the present context, legumain plays important roles in tumorigenesis and metastasis [28,30]. Several studies have shown that legumain is highly expressed in many kinds of solid tumors including colorectal [31], breast [32], ovarian [33], prostate [34] and gastric cancers [35]. Owing to the overexpression of legumain in tumor environments, it has been considered an ideal biomarker for tumor targeting. Functionally, legumain is involved in cell signaling related to cell (tumor) growth and migration [36]. Legumain is active in the degradation of the extracellular matrix and forms a proteolytic network that interacts with other tumor-promoting or suppressing biomolecules. Legumain's proteolytic activity shows high specificity toward the asparaginyl P1 site of the substrate [28]. It uses a nucleophilic amino acid sidechain to catalyze the hydrolysis of the peptide substrate [37,38]. It is now well established that legumain forms as a catalytically inactive zymogen (prolegumain in mammals; 56 kDa) that undergoes autocatalytic processing under low pH (acidic conditions) to produce two intermediate species (47 kDa and 46 kDa). When the intermediate legumain binds to asparaginyl via a carboxypeptide bond, it transforms into a mature, active form (36 kDa) [28].

The pH sensitivity of prolegumain makes it a highly useful biomolecule in tumor microenvironments [33], allowing targeting with legumain-specific peptides. Legumain has a very narrow substrate specificity, cleaving selectively after asparagine residues, allowing the use of legumain-selective peptides to target the tumor microenvironment.

In a recent study, the relative legumain-targeting efficiency of a 10-mer linear peptide and its Y-shaped equivalent [39] having the same amino acid sequence was investigated using computer simulations and *in vitro* experiments on cell types with varying levels of legumain expression, such as RAW 264.7, 4T1, MCF 10 A, MCF 7 and MDA MB 231 cells [40]. The linear peptide had a higher legumain binding efficiency in legumain-active cells compared with the Y-shaped peptide. Here, the authors prepared and utilized pSi NPs functionalized with 10-mer linear and Y-shaped peptides, abbreviated here as LPep_pSi and YPep_pSi, respectively, as fluorophores for targeting legumain using *in vitro* experiments. The better-performing peptide–pSi NPs formulation was further tested for *in vivo* legumain-binding affinity through *ex vivo* fluorescence imaging of excised organs using a syngeneic mouse model of breast cancer.

Materials & methods

Preparation of pSi, LPep_pSi, & YPep_pSi NPs

pSi NPs with a pore size of $\sim 10.0 \pm 7.2$ nm were prepared via electrochemical etching (at 21.8 mA cm^{-2}) of a B-doped silicon wafer in 3:1 HF-ethanol solution. Perforations were made at 90.9 mA cm^{-2} to facilitate the fracturing of the wafer into pSi NPs. The electropolished pSi membranes were lifted and ultrasonicated in dimethyl sulfoxide (DMSO) for 16 h to produce pSi NPs with oxidized surfaces. The pSi NPs were filtered through a 0.2-μm nylon filter membrane, vacuum dried and stored in a vacuum container to avoid further oxidation. Aliquots of the NPs in absolute ethanol (1 mg ml^{-1} concentration) were prepared and stored.

The linear peptide (LPep; NH$_3$-FITC-Ahx-Lys-His-Lys-His-Lys-His-Leu-Asn-Ala-Ala-COOH-terminal; Figure 1A) was purchased from Biomatik Peptide Services (Kitchener, Ontario, Canada) and the Y-peptide (YPep; NH$_3$-(FITC-Ahx-Lys-His)$_2$-Lys-His-Leu-Asn-Ala-Ala-COOH-terminal; Figure 1B) was purchased from GenScript (Seri Kembangan, Selangor, Malaysia). The peptides were tagged with fluorescein isothiocyanate (FITC) for flow cytometry.

To investigate targeting efficiency, the two peptides were conjugated to pSi NPs through a slightly modified microwave-assisted method [41]. Briefly, 100 μl of peptide (1 mg ml^{-1}) was added to 100 μl (100 μg ml^{-1}) of pSi NPs in ultrapure water. The mixture was heated using pulsed microwave irradiation (30 s) at 35°C for 10 min. The unbound peptide was removed as supernatant in three cycles of centrifugation (22,000 r.p.m. for 5 min; Figure 2). The pellet containing the peptide-conjugated pSi NPs was lyophilized for 8 h before use in for further studies.

Characterization of pSi, LPep_pSi & YPep_pSi NPs

The hydrodynamic size and zeta potential values of the as-prepared and peptide-conjugated pSi NPs were obtained via dynamic light scattering (DLS) using a zetasizer (Malvern Instruments, Malvern, UK). Particle size was also measured using field-emission scanning electron microscopy, (FESEM; Hitachi SU8010, Tokyo, Japan). The functional groups present in the NPs were identified using Fourier-transform infrared (FTIR) spectroscopy (Varian Instruments, CA, USA). The PL spectra of pSi, LPep_pSi and YPep_pSi NPs were obtained using Raman spectroscopy (Horiba, Loos, France) under He-Cd UV laser excitation (325 nm) and fluorescence images were obtained using a scanning laser confocal microscope (Nikon, Tokyo, Japan) at excitation wavelengths of 488 nm and 538 nm. All data reported are averages of triplicate measurements of samples obtained in three separate preparations.

NP stability

The stability of the pSi, LPep_pSi and YPep_pSi NPs under varying pH (2–10), temperature (25–65°C) and medium composition (ultrapure water, phosphate-buffered saline [PBS], human serum, human plasma and DMEM) was monitored using Zetasizer hydrodynamic size: 500 μl of NP formulation in ultrapure water (1 mg ml^{-1}) was dispersed in 500 μl each of pH solution mixed using a shaking water bath at room temperature for 5 min before measurement. The temperature was maintained at 25°C. For thermal stability, NP solutions were incubated in ultrapure water at pH 7.0 at fixed temperatures for 5 min in a shaking water bath before the size measurement. The stability of the NPs in various media at 25°C was also obtained by dispersing 500 μl (1 mg ml^{-1}) NPs in 500 μl of medium at pH 7.0. Finally, the stability of the formulations was also studied under physiological conditions by dispersing 500 μl of NPs (1 mg ml^{-1}) in 500 μl of PBS (pH = 7.4) at physiological temperature (37°C) in a
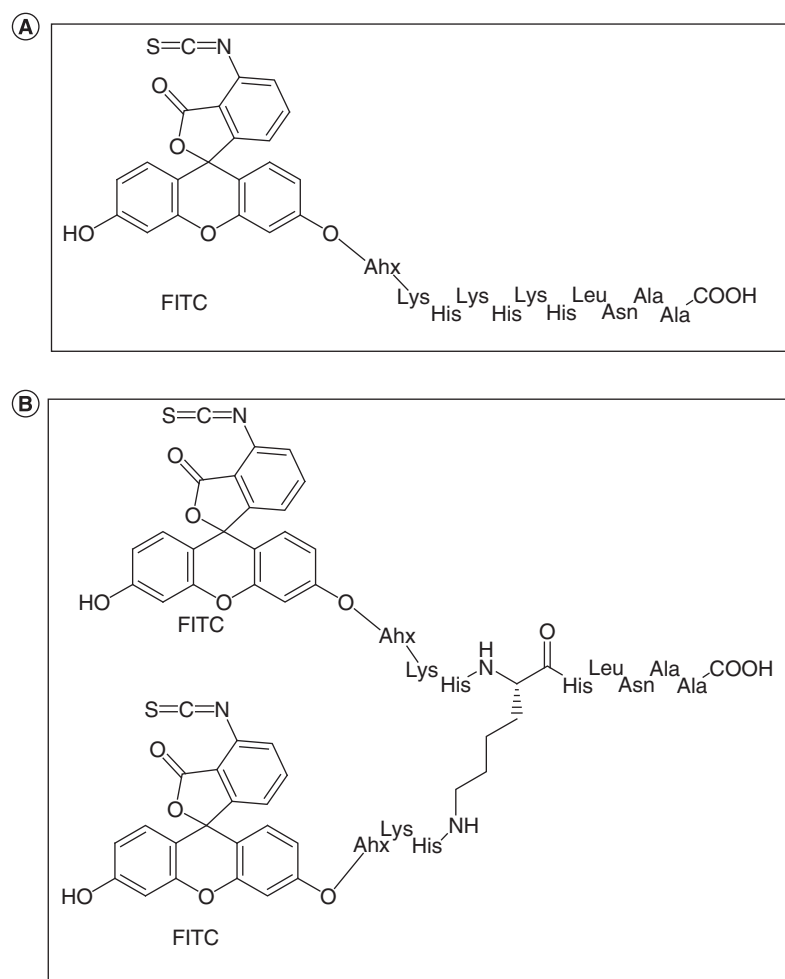
Figure 1.   Chemical structures of (A) LPep and (B) YPep.
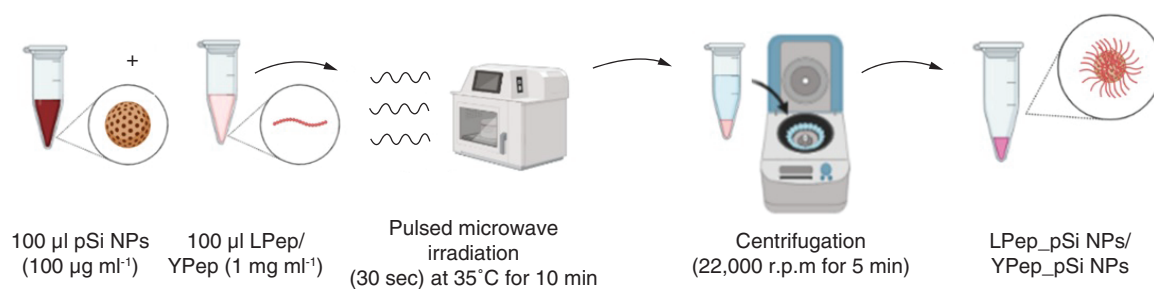Figure reproduced from [40].

Figure 2.   Preparation of LPep‑pSi, and YPep‑pSi nanoparticles.
Figure created using BioRender.com.
LPep: Linear peptide; LPep pSi NPs: Linear peptide conjugated porous silicon nanoparticles; pSi NPs: Porous silicon nanoparticles; YPep: Y-shaped peptide; YPep pSi NPs: Y-shaped peptide conjugated porous silicon nanoparticles.

shaking water bath. Hydrodynamic size measurements were taken at 0, 10, 30, 60, 90 and 120 min to investigate time-dependent stability. The stability data reported are averages of triplicate Z-readings.

Cell culture

RAW 264.7 (ATCC TIB-71, murine macrophage cells), MCF 7 (ATCC HTB-22, human mammary gland adenocarcinoma cells), MDA MB 231 (ATCC HTB-26, triple-negative human mammary gland adenocarcinoma cells) and 4T1 (ATCC CRL-2539, mouse mammary gland stage IV carcinoma cells) were cultured in DMEM (Sigma-Aldrich, MO, USA) supplemented with 10% fetal bovine serum (Gibco BRL, NY, USA) and 1% penicillin-streptomycin (PS) solution (Gibco BRL). MCF-10A (human mammary gland cells) were cultured in DMEM containing 5% horse serum (Gibco BRL), 10 µg ml^{-1} human insulin (Sigma-Aldrich), 20 ng ml^{-1} EGF (Sigma-Aldrich), 0.5 µg ml^{-1} hydrocortisone (Sigma-Aldrich) and 1% PS solution (Gibco BRL). The cultured cells were incubated in T75 flasks (Cole-Parmer, IL, USA) at 37°C in a humidified incubator supplied with 5% CO_2.

In vitro cytotoxicity

The cytotoxicity of the NP formulations was evaluated on five cells, including RAW 264.7, MCF 7, MDA MB 231, 4T1 and MCF 10A (ATCC CRL-10317, nonmalignant mammary gland epithelial cells), using the 3-(4,5-dimethylthiazol-2-yl)-2,5-diphenyl tetrazolium bromide (MTT; Sigma-Aldrich) cell proliferation assay. The cells were seeded in a 96-well plate (1 × 10^4 per well) and incubated at 37°C overnight in a humidified incubator supplied with 5% CO_2 to allow cell attachment to the walls. The next day, the spent culture medium was removed from all wells and cells were gently washed with PBS. Various amounts of NPs in fresh DMEM (200, 100, 50, 25, 12.5, 6.3, 3.2, 1.6, 0.8 and 0 µg ml^{-1}) were then added to assigned wells and the plate was incubated at 37°C in a humidified incubator supplied with 5% CO_2 for 24 or 48 h. After incubation, the NP solution was removed and 50 µl of freshly prepared MTT solution (0.5 mg ml^{-1}) was added to each well. The plates were kept in the incubator for a further 4 h. Next, 100 µl of DMSO was added to each well. Absorbance reading at 570 nm was obtained immediately using a spectrophotometer (BioTek, VT, USA). The experiment was repeated three times with triplicate readings in each run.

Cellular association

Cellular association was studied for RAW 264.7 and 4T1 cells. The cells were seeded (1 × 10^6 cells per well) in 6-well plates with sterile coverslips and incubated overnight at 37°C in a humidified incubator supplied with 5% CO_2 to allow them to attach to the coverslip. The medium was removed and 200 µg ml^{-1} of pSi, LPep_pSi or YPep_pSi was added to the respective wells and incubated at 37°C for 12 h. The cells were washed with PBS and fixed with 4% paraformaldehyde for 20 min. The cells were then incubated with allophycocyanin (APC; Novus Biological, CO, USA)-tagged antilegumain antibody (R & D Systems) for 12 h. The cells were washed with PBS and fixed with paraformaldehyde for 20 min. Excess fixing agents were washed with PBS each time. Cells were stained with 4′,6-diamidino-2-phenylindole (DAPI) (0.3 µg ml^{-1}) for three s, after which coverslips were washed with PBS and mounted onto slides. The slides were viewed and imaged using a laser scanning confocal microscope (Nikon) with 488 nm and 538 nm excitation filters.

Fluorescence-activated cell sorting

The targeting of legumain present on RAW 264.7, 4T1, MCF 7 and MCF 10A cells by pSi, LPep, YPep, LPep_pSi and YPep_pSi was evaluated using fluorescence-activated single cell sorting (FACS) flow cytometry. The FITC-tagged peptides were used for FACS. A total of 100 µg ml^{-1} of pSi, peptide, LPep_pSi or YPep_pSi was added to 5 ml tubes containing 1 × 10^6 cells, and the tube was vortexed and incubated in the dark for 30 min at room temperature. The cells were then washed in cold PBS, recovered by centrifugation and gently resuspended in the residual PBS. Next, 2 µg ml^{-1} of antilegumain primary antibody was added to all tubes, which were then briefly vortexed and incubated in the dark for 15 min. Cells were washed three times and gently resuspended in the remaining PBS. A secondary antibody that binds to APC-tagged antilegumain antibody was added to each tube and the tubes were vortexed and incubated in the dark for 15 min. After repeated washes, cells were gently resuspended in 300 µl of cold stain buffer (BD Biosciences, NJ, USA) and analyzed immediately using FACSVerse flow cytometer (BD Biosciences) with laser excitation (y = 488 nm and 600 nm). A total of 10,000 events were recorded for each sample. The experiment was repeated twice with triplicate samples for each cell line. Data analysis was performed using ModFit LT^{TM} Version 4.0 software (Verity Software House, ME, USA).

In the present work, legumain expression was not measured using techniques such as western blot or reverse transcription PCR (RT-PCR), since previous studies have tested legumain expression in the cell lines used in this

study. It is well established that legumain shows weak expression in cultured (*in vitro*-grown) cell lines, except in macrophage cells [42].

Animal study

The tumor-targeting efficiency of the NP formulations was evaluated using a syngeneic mouse model of breast cancer. The animals used were 6–8 weeks old female BALB/c mice sourced from the Animal Holding Facility (Monash University, Bandar Sunway, Malaysia). Animals were closely monitored and had access to food and water *ad libitum*. Six mice each (n = 6) were randomly assigned to three experimental groups. Breast cancer was induced through orthotopic injection of 1×10^6 4T1 cells into the left flank of the mouse breast pad. The 4T1 cells were chosen for the animal study because the growth and metastatic spread of 4T1 cells in BALB/c mice are known to closely mimic human breast cancer [42]. The tumor was palpable (average diameter: 5 mm; volume: ∼65 mm³) 14 days postinoculation. All animal work was carried out in accordance with the institutional animal protocol guidelines provided by the Animal Ethics Committee (Monash University, Clayton, Australia; AEC number: MARP/2017/004).

Ex vivo fluorescence imaging

The biocirculation of pSi and LPep‗pSi NPs in the tumor-induced mice was monitored using *ex vivo* fluorescence. LPep‗pSi was chosen (instead of YPep‗pSi) as the functionalized nanovector due to its higher aqueous stability and established higher *in vitro* legumain-targeting efficacy (see below and [40]). PBS (control), pSi or LPep‗pSi was injected intravenously into the tail vein of mice with palpable tumors. After 4 or 24 h, the mice were euthanized by exposure to an overdose of CO_2. At autopsy, organs (brain, heart, spleen, kidneys, lungs, stomach and liver) and tumor tissue were harvested and preserved in ice. Organs were imaged *ex vivo* using MS FX PRO equipment (Bruker, Bremen, Germany) at the Animal Experimental Unit (University Malaya, Kuala Lumpur, Malaysia). The fluorescence was measured using 690 nm excitation and 730 nm emission filters. The fluorescence intensity was subtracted from the background value to obtain quantitative data. Data and image analyses were carried out using Carestream Molecular Imaging software (Bruker, MA, USA).

Histopathology

Histopathology was carried out on the organs and tumor tissues. The organs were fixed in a 10% neutral-buffered formalin solution, tissue processed (Leica, Wetzlar, Germany), embedded in paraffin wax and stored at 4°C. Sections (3–4 μm) of sample-embedded paraffin blocks were placed on frosted glass slides and heated at 30–35°C for 10 min on a hotplate. The wax was removed by immersing (2 × 1 min) the slides in xylene and cleared using ethanol. The slides were then immersed in water and stained in hematoxylin (H) solution for 4–8 min. The slides were rinsed with water, immersed in acid–alcohol solution for 2–3 s, rinsed with water again and dipped in bicarbonate solution (the sections turned blue). The slides were again rinsed with water, immersed twice in 95% alcohol and stained in eosin (E) for 2 min. The slides were then soaked in 95% alcohol twice for 30 s each and rinsed with two changes of absolute alcohol. Alcohol was removed with two changes of xylene at 30 s each. The slides were kept in Clearene until covered with coverslips. Light microscopy analysis (Eclipse TS100; Nikon) of the prepared slides was conducted by a pathologist blinded to the study. The slides were evaluated for various pathological features (e.g., inflammation, congestion). Photomicrographs were taken using a Nikon 8.1 MP camera (Nikon) and analyzed using Nikon Eclipse software.

Statistical analysis

Statistical analysis of the hydrodynamic size data for the NPs under varying pH, temperature, medium and time conditions as well as the fluorescence intensity data for pSi and LPep‗pSi NPs at 4 h and 24 h were analyzed by Student's *t*-test using GraphPad Prism 5.0 for Windows (GraphPad Software, CA, USA; www.graphpad.com). Statistically significant differences are defined as: *$p < 0.05$; **$p < 0.01$ and ***$p < 0.001$; ns (no significance).

Results
Characterization of NPs

The pSi, LPep‗pSi and YPep‗pSi NPs had approximately equant morphology (Figure 3A–C). The particle sizes of pSi obtained with FESEM, ∼50–60 nm, were close to the average DLS hydrodynamic size of 89 ± 2 nm (Figure 3A
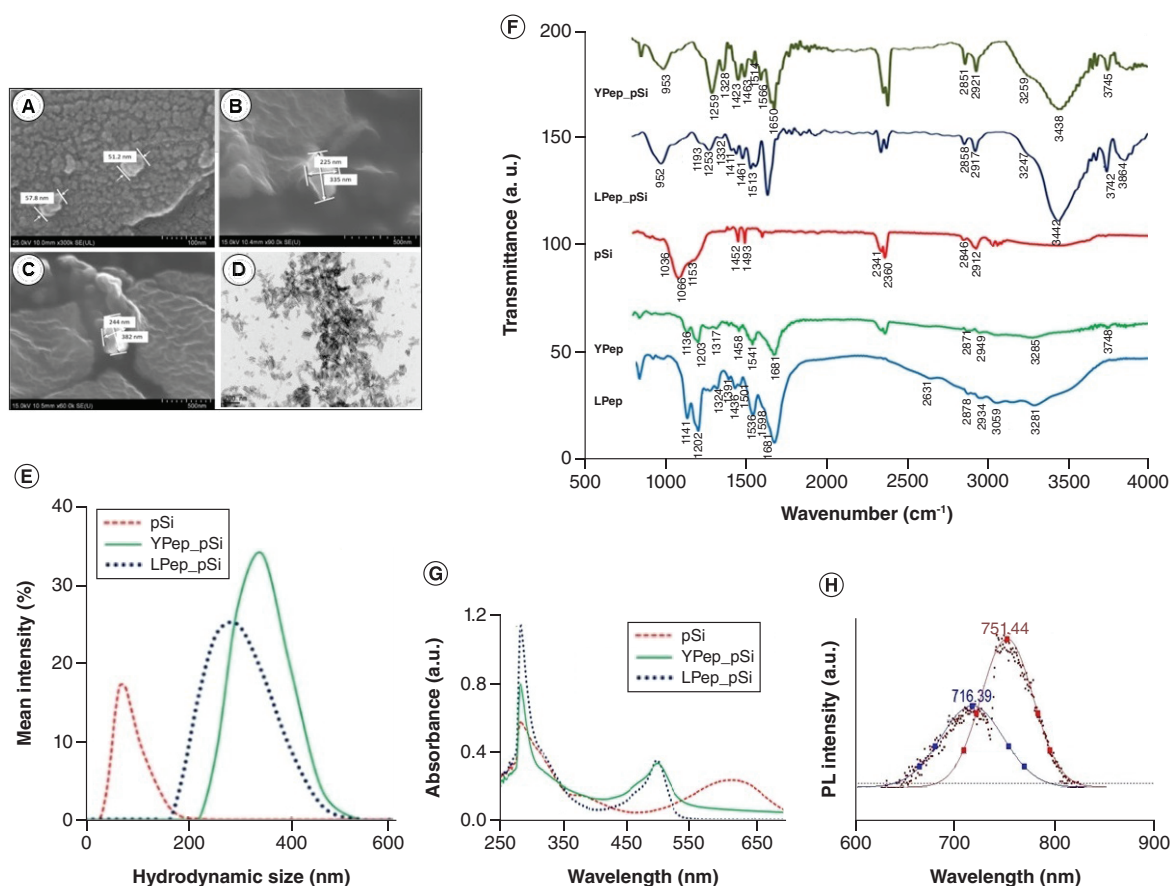
Figure 3.   Characterization of the nanoparticles. Field-emission scanning electron microscopy image of **(A)** pSi, **(B)** LPep_pSi and **(C)** YPep_pSi. **(D)** Transmission electron microscopy image of pSi. **(E)** Hydrodynamic size distribution of pSi, LPep_pSi and YPep_pSi nanoparticles obtained with dynamic light scattering. **(F)** FTIR spectra of pSi, LPep, YPep and peptide-functionalized pSi NPs (YPep_pSi and LPep_pSi). **(G)** UV-visible absorption spectrum of pSi and peptide-functionalized pSi (YPep_pSi and LPep_pSi). **(H)** The "slow" (S)-band NIR PL emission of pSi resolved into two peaks.
Excitation λ = 325 nm.
LPep: Linear peptide; LPep_pSi: Linear peptide conjugated porous silicon; pSi: Porous silicon; YPep: Y-shaped peptide; YPep_pSi: Y-shaped peptide conjugated pSi.

& E). The transmission electron microscopy (TEM) image of the pSi NPs (Figure 3D) showed crystallites with a porous structure. Similarly, the DLS hydrodynamic sizes of LPep_pSi (295 ± 15 nm) and YPep_pSi (325 ± 21 nm) were close to the average particle size measured with FESEM: 225 nm × 335 nm for LPep_pSi and 244 nm × 382 nm for YPep_pSi (Figure 3B, C & E). The zeta potential values (in mV) for pSi, LPep_pSi and YPep_pSi were -112.47 ± 2.30, -26.83 ± 1.32 and -19.83 ± 1.35, respectively.

Figure 3F shows the FTIR spectra of pSi, LPep, YPep, LPep_pSi and YPep_pSi. The FTIR spectrum of pSi showed absorption bands due to Si–O–Si (1000–1200 cm^{-1}), Si–OH ($\sim$1036 cm^{-1}), C–H (1452 and 1493 cm^{-1}), Si–CH$_3$ (2846 and 2912 cm^{-1}) and OH ($\sim$3450 cm^{-1}) vibrations, suggesting pSi NPs with ultrathin silica coating and residual hydrocarbons acquired from the preparation [5,43,44]. The 2341 cm^{-1} and 2360 cm^{-1} bands were due to the spectrometer atmosphere. The FTIR spectra of the peptides showed characteristic amide I (C=O stretching $\sim$1650 cm^{-1}), amide II (in-plane N-H bending at $\sim$1540 cm^{-1}) and amide III (C–H had in-plane bending, C–N symmetric stretching and O–H in-plane bending and molecular bond stretching at 1130–1390 cm^{-1}) vibrations [45,46]. Major changes were seen in the FTIR spectra of peptide-functionalized pSi NPs in the 1000–1200 cm^{-1} region including suppression of the Si–O–Si and Si–OH bands in pSi and the amide III bands in the peptides.

The UV-visible (UV-Vis) light absorption spectra of pSi and peptide-functionalized pSi (Figure 3G) suggest a sharpening and blueshift of the $\sim$600 nm pSi absorption maximum to $\sim$500 nm upon functionalization. Figure 3H
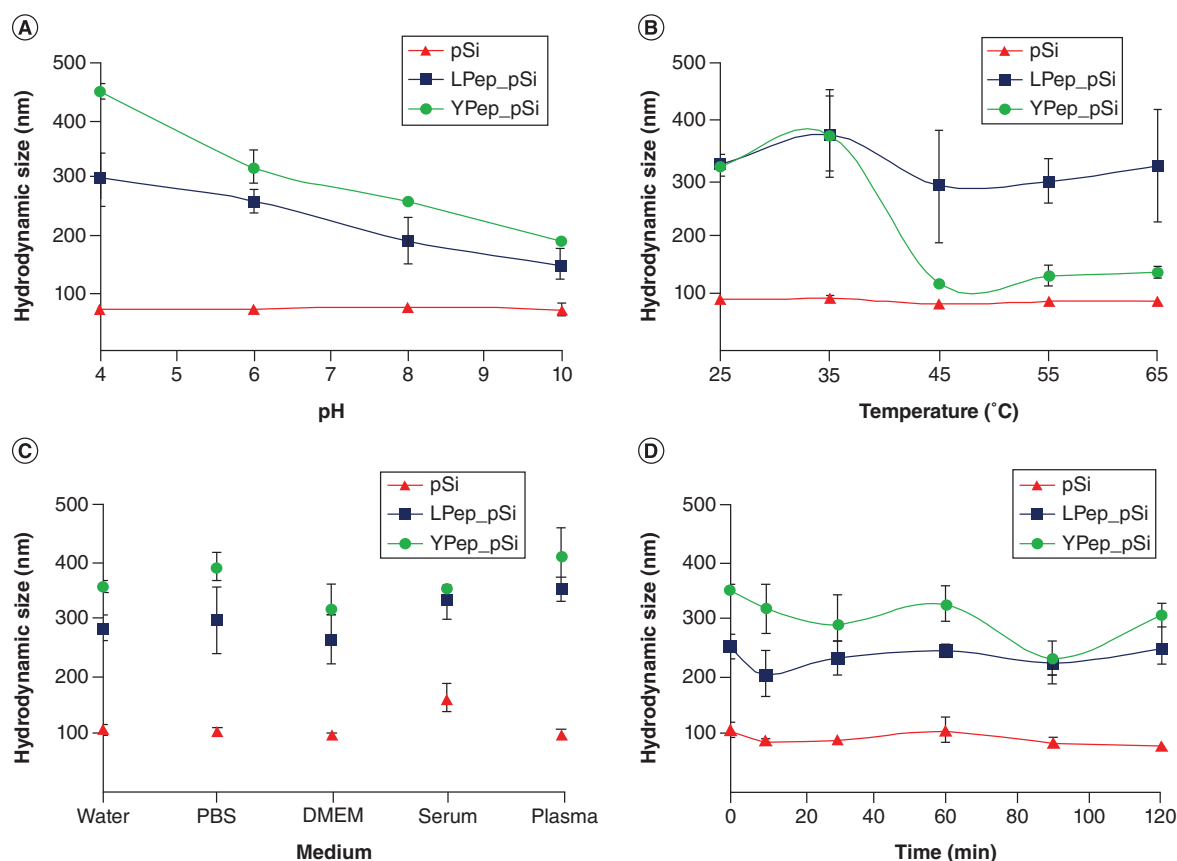
Figure 4.   Stability of the nanoparticle formulations. Stability of pSi, LPep_pSi and YPep_pSi nanoparticles with varying **(A)** pH, **(B)** temperature, **(C)** medium composition and **(D)** duration in phosphate-buffered saline monitored using hydrodynamic size.
DMEM: Dulbecco's Modified Eagle's Medium; LPep_pSi: Linear peptide-conjugated porous silicon; PBS: Phosphate-buffered saline; pSi: Porous silicon; YPep_pSi: Y-shaped peptide-conjugated porous silicon.

shows the red ("slow" or S-band) PL emission band from pSi NPs produced by UV laser (λ = 325 nm) excitation due to the native oxide layer. (The "fast" blue-green PL emission in batches of pSi particles stored in the laboratory were also observed.) Although photon absorption is affected by peptide functionalization (Figure 3G), the PL emission wavelength was unaltered by it. The S-band PL emission usually appears as a broad peak. However, this Raman-PL data obtained under low laser power was resolvable into two Gaussian + Lorentzian peaks, suggesting multiple PL emission peaks, possibly caused by polydispersity or aging effects [47,48].

Stability of NPs

The average hydrodynamic size of the pSi NPs remained nearly constant with varying pH, temperature, medium composition and duration in PBS (Figure 4). The LPep_pSi NPs show a size decrease with increasing pH from ∼300 nm at pH of 4 to ∼200 nm at pH of 10 (Figure 4A). These NPs are, however, stable across the range of temperatures, medium compositions and durations investigated (Figure 4B–D). The YPep_pSi NPs showed significant ($p < 0.05$) instability above ∼35°C; otherwise, they showed similar trends to the LPep_pSi NPs.

In vitro cytotoxicity of pSi, LPep_pSi & YPep_pSi NPs

The cytotoxicity of the pSi, LPep_pSi and YPep_pSi NP formulations was evaluated on five cell lines (4T1, MCF 7, MDA MB 231, MCF 10A and RAW 264.7) using the MTT cell proliferation assay. The results are plotted in Supplementary Figure 1. Cell viability of >70% was observed for all the cell types incubated with the NP formulations for 48 h (Supplementary Figure 1), suggesting that the NPs were nontoxic to the cells. No dose-dependent trends were observed, even at the highest concentration (200 μg ml⁻¹) tested, indicating that the NP preparations were safe. Previous studies have also shown that pSi is nontoxic to RAW 264.7 cells [49].
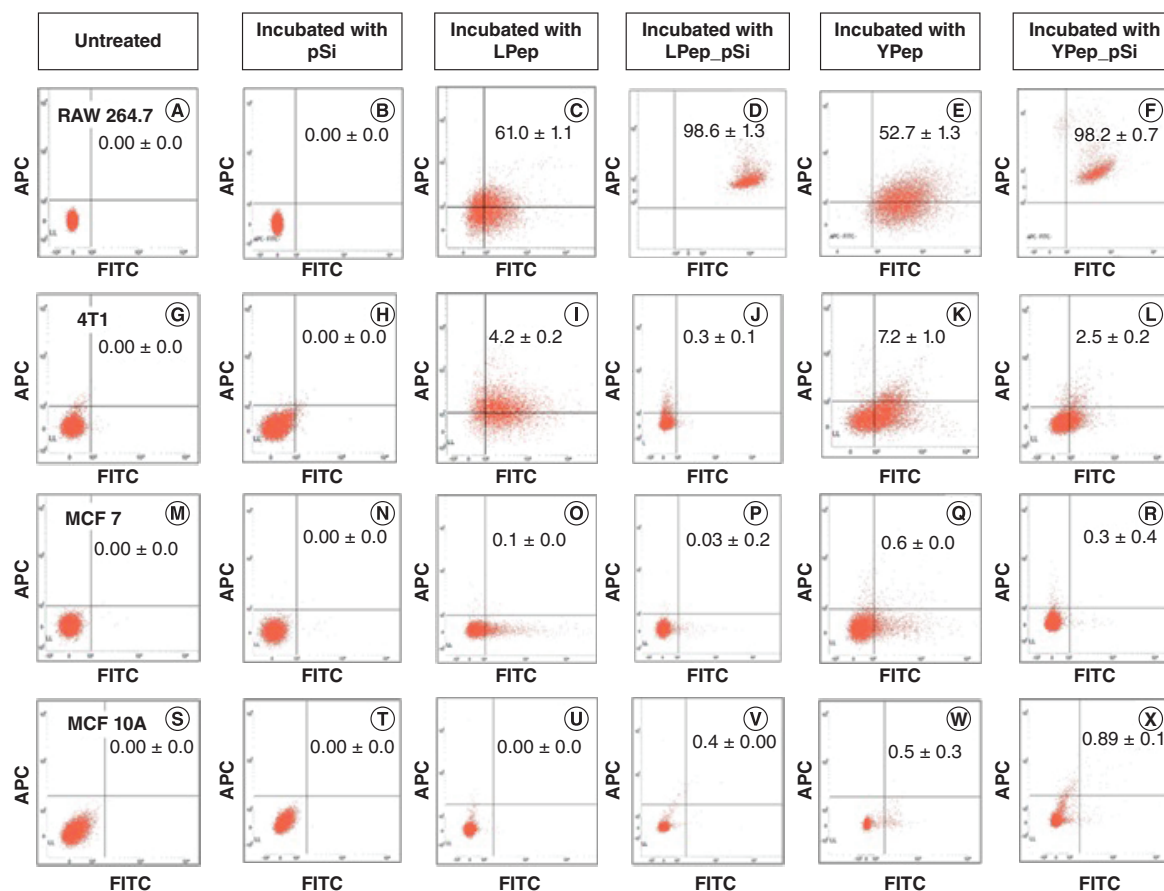
Figure 5. Fluorescence-assisted cell sorting analysis of RAW 264.7, 4T1, MCF 7 and MCF 10A cells in unstained condition and incubated with pSi, LPep, YPep, LPep_pSi and YPep_pSi nanoparticles.
APC: Allophycocyanin; FITC: Fluorescein isothiocyanate; LPep_pSi: Linear peptide-conjugated porous silicon; pSi: Porous silicon; YPep_pSi: Y-shaped peptide-conjugated porous silicon.

In vitro legumain-targeting efficiency of NPs

FACS was used to quantify the legumain-targeting efficiency of the LPep, YPep, LPep_pSi and YPep_pSi formulations in relation to four cell types: cells with high legumain expression (RAW 264.7) and cells that express low or zero legumain (MCF 7, 4T1 and MCF 10A). The four cell types incubated with pSi NPs were also used for comparison. Binding of FITC-conjugated peptide present in the formulations to the active site of legumain results in legumain-peptide interaction, which activates the legumain biomarker. The legumain activity on the cells was recognized using APC fluorescence while FITC fluorescence allowed recognition of peptide binding. The binding of the peptide at the carboxyl-bonded asparaginyl site activates legumain at acidic pH [28]. The active form of legumain is bound by an antilegumain primary antibody that has high specificity toward activated legumain. The antilegumain primary antibody binding to legumain on the cell surface was detected using an APC-tagged secondary antibody. Double-positive population (upper-right quadrant) events in Figure 5 representing two-color fluorescence (from FITC and APC) quantify the targeting efficiency of the peptides in relation to legumain on the cells.

The control sample (untreated cells) and cells incubated only with pSi NPs clearly showed no legumain binding in the four cell types (Figure 5). The maximum legumain targeting (52.7–98.6%) was obtained for RAW 264.7 macrophage cells treated with peptide-containing formulations while 4T1 cells appear to have had very low cell surface expression of legumain, with targeting efficiency <7.2 ± 1%. Similarly, cultured MCF 7 breast cancer cells show extremely low legumain targeting (0.03–0.6%). Finally, in the case of nontumor MCF 10A cells, statistically insignificant targeting efficiency was obtained, as expected.
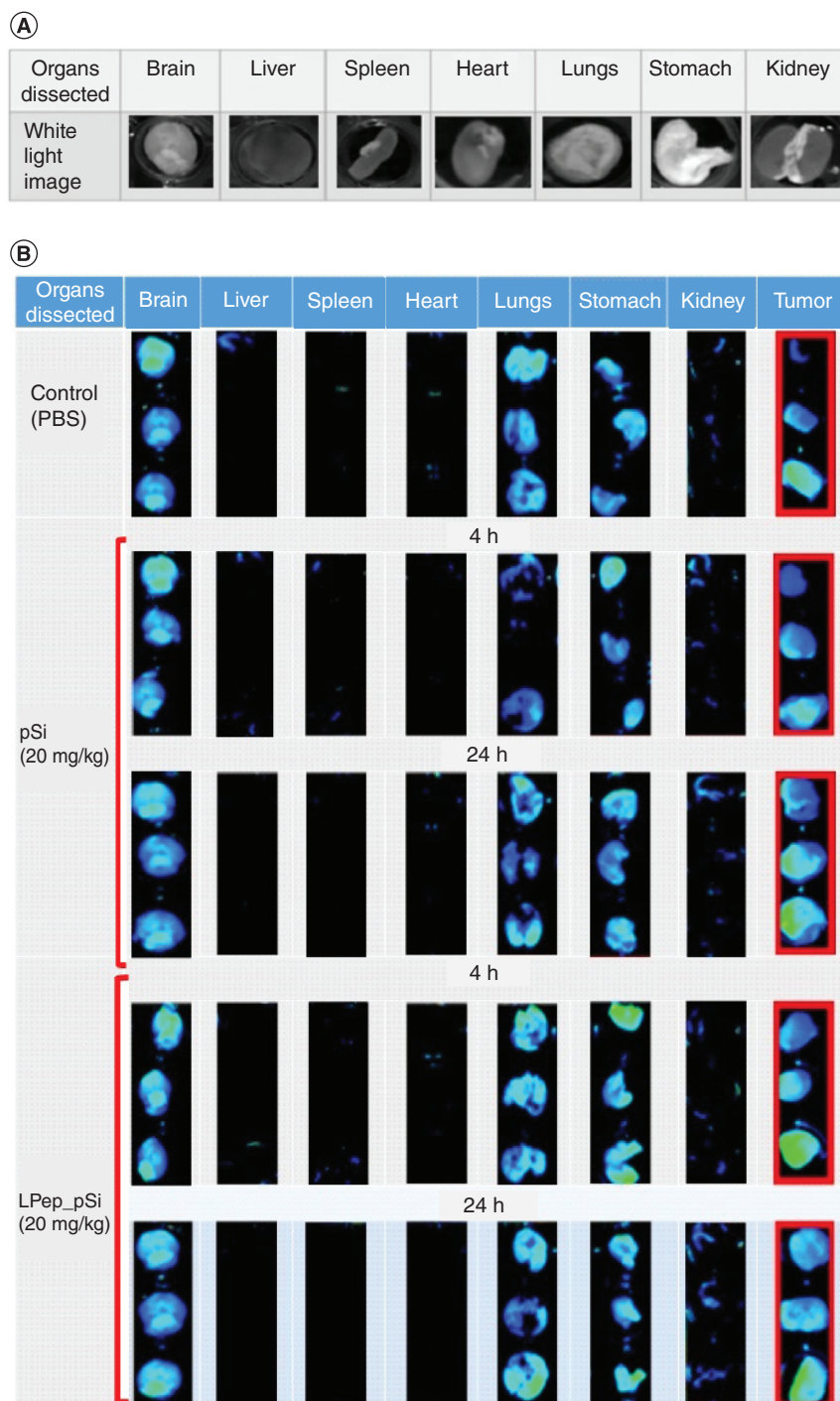
Figure 6.   *Ex vivo* fluorescence images of various extracted organs. (A) White light (greyscale) image of various excised mouse organs. **(B)** *Ex vivo* fluorescence images obtained from the organs of control (phosphate-buffered saline)-, porous silicon nanoparticles- and linear peptide-conjugated porous silicon nanoparticles-injected tumor-induced mice. Tumor tissues are shown in red boxes in **(B)**.
LPep_pSi: Linear peptide-conjugated porous silicon; PBS: Phosphate-buffered saline; pSi: Porous silicon.

Ex vivo imaging of pSi & LPep_pSi NP biodistribution

Ex vivo imaging showed no illumination under white light and insignificant fluorescence from the liver of NP-injected mice (Figures 6 & 7). As with thermally hydrocarbonized pSi NPs [18], the present oxidized pSi NPs accumulated in the kidney (scaled fluorescence intensity: ~1.31×10^7 pW mm^{-2}) and tumor (scaled fluorescence
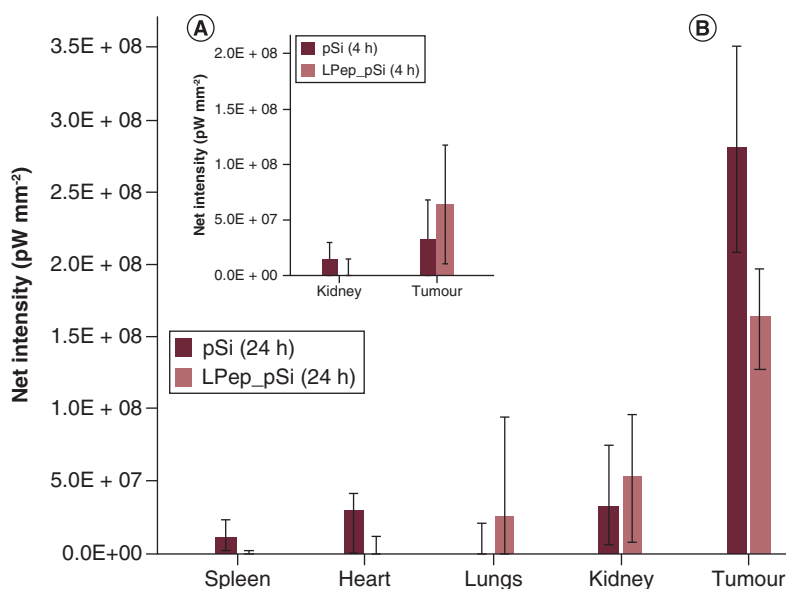
Figure 7.   Fluorescence intensity distribution in various organs of tumor-induced mice injected with pSi or LPep_pSi nanoparticles after 4 and 24 h (p < 0.05).
LPep_pSi: Linear peptide-conjugated porous silicon; pSi: Porous silicon.

intensity ∼3.13 × 10^7 pW mm^{-2}) within a relatively short time (Figure 7A). By 24 h, among the organs examined, fluorescence (suggesting accumulation of pSi NPs) was seen in the spleen (1.07 × 10^7 pW mm^{-2}), heart (3.02 × 10^7 pW mm^{-2}) and kidney (3.19 × 10^7 pW mm^{-2}), whereas the brain and lungs did not show significant fluorescence. Notably, tumor tissue showed the highest fluorescence intensity due to pSi NPs (scaled intensity: 28.0 × 10^7 pW mm^{-2}). A ninefold increase in the fluorescence signal due to the gradual build-up of pSi NPs was observed in tumor tissues between 4 and 24 h.

Fluorescence due to LPep_pSi NPs was observed only in the tumor region (6.37 × 10^7 pW mm^{-2}; p = 0.169) at 4 h (Figure 7A). At 24 h, fluorescence at the tumor increased 2.5-fold (16.34 × 10^7 pW mm^{-2}; p = 0.379). Fluorescence was also observed in the kidneys (5.24 × 10^7 pW mm^{-2}) and lungs (2.58 × 10^7 pW mm^{-2}) at the 24 h mark.

Histopathology analysis

Histopathological changes in various organs of animals treated with pSi or LPep_pSi NP formulations for 4 and 24 h (n = 3 per group and per timepoint) were examined. Tumors excised from tumor-induced animals were also analyzed. Untreated tumor-induced animals served as controls. The essential histopathological changes observed in the liver, lungs and tumor and histopathology of other organs were as follows. The liver from the control group (Figure 8A) and nontumor-induced animals (not shown) showed normal architecture with central vein and well-spaced portal triads, mild inflammatory cells and congestion. Hepatocytes and sinusoids appeared normal. Numerous micrometastatic deposits were present in the liver of control group animals, both in the parenchyma and along the vessels. For the pSi NP-injected groups (Figure 8B), the liver showed areas of congestion and inflammation in all three groups of nontumor-induced and tumor-induced animals at 4 h (T4) and 24 h (T24). The central veins were dilated and congested. The portal triad and sinusoids showed mild dilatation with scattered inflammation. Hepatocytes appeared normal. Numerous micrometastatic deposits were present only in the T24 group, both in the parenchyma and along the vessels. In LPep_pSi NP-treated animals, the liver showed areas of congestion and inflammation in the nontumor, T4 and T24 (Figure 8C) groups. The central veins were dilated and congested. The portal triad and sinusoids showed mild dilatation with scattered inflammation. As in the livers of pSi NP-treated animals, hepatocytes appeared normal in the livers of LPep_pSi NP-treated animals. Again, micrometastatic deposits of the tumor were present only in the T24 group, both in the parenchyma and along the vessels.

In control mice, the lungs showed normal alveoli and bronchiolar spaces. No metastatic deposits or inflammation were noted (Figure 8D). In the pSi NP-treated nontumor group and T24 group (Figure 8E), the lungs showed
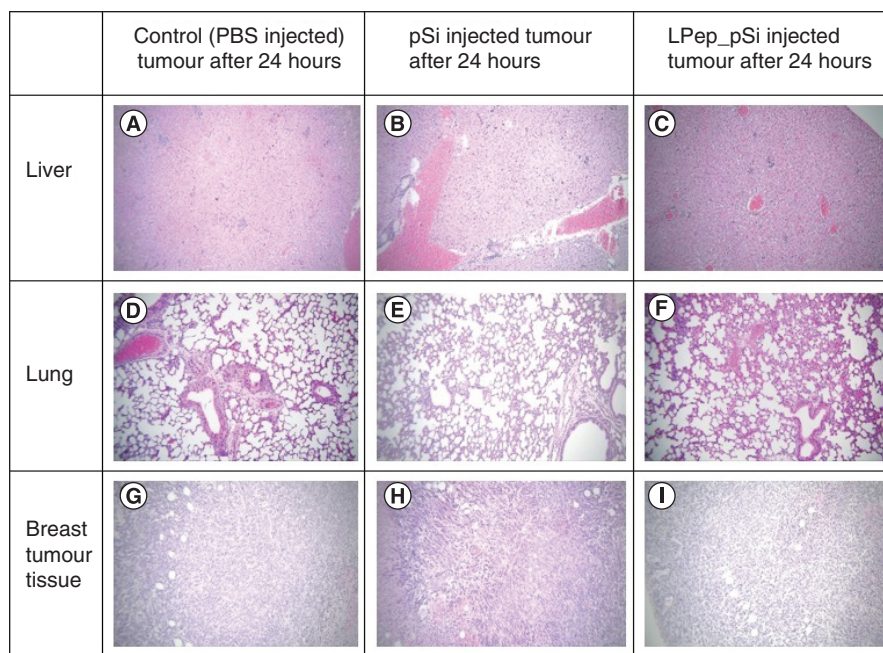
Figure 8.   Histopathology of selected tissues. Sections (100× magnification) showing **(A–C)** liver, **(D–F)** lung and **(G–I)** breast tumor tissue.
All animals were euthanized 24 h postinjection and tissues were stained with hematoxylin and eosin dye.
LPep_pSi: Linear peptide-conjugated porous silicon; PBS: Phosphate-buffered saline; pSi: Porous silicon.

normal alveoli and bronchiolar spaces. No metastatic deposits or inflammation were noted. In the T4 group (not shown), the lungs showed focal areas of edema and congestion. In all three groups of LPep_pSi NP-treated samples, the lung showed normal alveoli and bronchiolar spaces with focal areas of edema and congestion. No metastatic deposits or inflammation were noted (Figure 8F).

The control group's primary breast tumor tissue showed clear areas of necrosis in the tumor sections (Figure 8G). The tumor was surrounded by fibrous stroma and extended into the neighboring soft tissue areas, and the cells were packed in sheets and clusters. In tumor sections from pSi NP- or LPep_pSi NP-treated animals at 4 h (not shown) and 24 h (Figure 8H & I), the tumor cells were large and showed hyperchromasia with clear areas of necrosis. Upon autopsy, enlargement of the spleen was observed. There were no morphological changes or damage observed in the cerebellum, cerebrum, spleen, heart or stomach (data not shown). Histopathological evaluations also suggested that the dose of pSi NPs and LPep_pSi NPs (20 mg/kg) used in the syngeneic mouse model of breast cancer was optimal and there were no significant signs of toxicity observed.

Discussion

The study objective of producing protease-targeting peptide-functionalized pSi NPs using a modified microwave-assisted method was successful, yielding LPep_pSi and YPep_pSi NPs, respectively, of 295 ± 15 nm and 325 ± 21 nm (DLS) size. The expected change in zeta potential upon peptide functionalization of the pSi NPs, due mainly to the presence of amino and carboxylic groups (in LPep_pSi and YPep_pSi NPs), was also borne out by the results. As is well known, the absolute zeta potential value obtained for pSi NPs varies considerably depending on the experimental parameters as well as NP characteristics such as pore size, porosity and surface chemistry [50]. The observed increase in the zeta potential values after peptide conjugation was similar to that reported in previous studies [18] and confirms effective attachment onto and complete coverage of the bare pSi NPs by the peptides. Further evidence of successful peptide attachment on the pSi NPs is provided by the FTIR spectra in the 1000–1200 cm⁻¹ region (Figure 3F): suppression of the Si-O-Si and Si-OH bands in pSi and the amide III bands in the peptides. Strong amide I vibrations at ~1650 cm⁻¹ (C=O stretching) in the FTIR spectrum suggest carboxylic acid groups on the NP surface [51] that can impart a negative charge upon losing the H atom, which eventually should favor longer circulation time in body fluids [52].

It is essential that the produced NPs possess desirable optical properties for their use in bioimaging. A reasonable light absorption profile was seen in the UV-Vis spectra of the three NP formulations, with a blueshift in the visible region absorption maximum after peptide functionalization (Figure 3G). The blueshift can be attributed to possible highest occupied molecular orbital - lowest unoccupied molecular orbital (HOMO-LUMO) energy gap modification due to peptide conjugation; the blueshift still allowed for adequate absorption in the blue–green region. Critically, the strong light absorption in the UV region (Figure 3G) and excellent PL emission in the NIR region (Figure 3H) make the functionalized NPs ideal for use in bioimaging using UV laser excitation. Notably, NIR light allows for deep-tissue penetration [7], which is highly desirable in bioimaging. Furthermore, the PL emission and cellular association characteristics of pSi and peptide-conjugated pSi NPs were also qualitatively studied using confocal microscopy on RAW 264.7 and 4T1 cells, and reasonable fluorescence due to efficient legumain-targeting was obtained for both cell types, supporting the bioimaging potential of the functionalized NPs [40].

In addition to possessing desirable optical properties, functionalized NPs should remain stable under varying environmental/temporal factors such as pH, temperature, medium and time within ranges relevant to bioapplications. The nearly constant hydrodynamic size of pSi NPs under varying pH, temperature, medium composition and duration in PBS (Figure 4) suggests a lack of significant surface modifications with varying conditions. Although pH had a small effect on the stability of LPep_pSi NPs, temperature, medium composition and time did not affect their stability significantly. This was not the case for the YPep_pSi NPs: temperature had a significant effect on their stability. The average hydrodynamic size of the YPep_pSi NPs approaching that of bare pSi NPs above ~35°C (Figure 4B) suggests peptide detachment from the YPep_pSi NPs at higher temperatures. Under more acidic conditions, the peptide-functionalized NPs are expected to be larger due to interactions between excess hydrogen (H^+) ions and the surface carboxylic group [53]. Plasma protein adsorption onto the NPs is an important factor controlling their stability and biocirculation under physiological conditions. Figure 4C shows that a statistically significant increase in the hydrodynamic size was not observed for the three NP formulations in human plasma medium, indicating insignificant plasma protein adsorption onto the NPs and suggesting NP stability. This agrees with previous studies that showed limited plasma protein adsorption on peptide/protein-coated NPs [18,54]. Furthermore, the particles were stable ($p < 0.05$) under physiological conditions (in PBS at 37°C) [Figure 4D]. Overall, the LPep_pSi NPs showed excellent stability across pH, temperature and medium compositions potentially encountered in bioapplications.

The legumain-targeting efficiencies of the different NP formulations obtained using *in vitro* FACS were in agreement with available published data. The RAW 264.7 macrophage cells with abundant legumain expression [38] showed the maximum legumain-targeting efficiency among the cell types studied. The lower targeting efficiency obtained for 4T1 mouse breast cancer cells can be understood in light of previous reports that cultured 4T1 cells have minimal or deficient legumain expression in contrast to 4T1 breast cancer cells in mice with high legumain expression [36]. A similar explanation can be advanced for the extremely low legumain targeting observed for MCF 7 human breast cancer cells. Several cultured tumor cell lines are reported to have low legumain expression compared with solid tumors in animal models due to serum starving and other factors in the tumor microenvironment [42]. Finally, in the case of nonlegumain-expressing, nontumor human mammary cells (MCF 10A), statistically insignificant targeting efficiency was obtained, as expected.

From the *in vitro* qualitative study of the cellular associations (confocal microscopy) of the NP formulations using two cell lines as well as quantitative FACS investigations using four cell lines, one can conclude that both LPep_pSi and YPep_pSi NPs have high legumain targeting efficiencies, and therefore, the peptide-pSi nanoformulations are useful for bioimaging of legumain-expressing cells. Overall, the results suggest that the linear peptide-conjugated formulation is a better choice for legumain targeting, in agreement with a previous report [40]. Moreover, LPep_pSi NPs showed relatively higher stability with varying temperature, pH, medium composition and time. Therefore, the animal model studies (discussed later) compare the biodistribution of pSi NPs and LPep-pSi NPs in a syngeneic breast cancer mouse model and the potential of both the NP formulations for bioimaging of legumain-expressing cells.

Biodistribution (including time-dependent biodistribution) and the eventual fate of parenterally and orally delivered bare and specifically functionalized pSi NPs in healthy and diseased syngeneic breast cancer mouse models are well established [5,18,49,54–59]. Intravenously administered oxidized pSi NPs (dosage: 20 mg kg^{-1}) accumulated mainly in the MPS organs, liver and spleen, within a day, biodegraded into silicic acid and fully eliminated in 4 weeks' time via renal clearance [5]. Bimbo *et al.* [49] demonstrated the different biodistribution pathways adopted by thermally hydrocarbonized, radio-labeled (^{18}F) pSi NPs that depended on the administration route. The pSi

NPs accumulated in the spleen and liver after intravenous delivery; however, the pSi NPs accumulated mostly in bone and the gastrointestinal tract when administered via subcutaneous and oral routes, respectively. Relatively higher amounts in the liver and spleen compared with kidneys of siRNA-loaded pSi NPs cleared from blood in 12 h via hepatobiliary and renal excretions [57]. In view of the well-established biodistribution patterns of pSi NPs in mouse models, the present study was principally focused on the biodistribution of pSi and LPep-pSi NPs in a tumor-induced syngeneic mouse model of breast cancer at 4 and 24 h (Figures 6 & 7). The absence of significant fluorescence in the liver of mice injected with pSi NPs and LPep_pSi NPs after 4 and 24 h (Figures 6 & 7) suggests rapid clearance. It has been demonstrated that negatively charged pSi NPs accumulate in the liver within 10 min of intravenous injection, then move to the duodenum after 60 min and are eventually excreted in the feces [60]. In the present study, the negatively charged pSi NPs and LPep_pSiNPs clearly evaded being entrapped by the MPS. Similar biodistribution results have been obtained at short durations for various functionalized pSi NPs in other studies as well.

Accumulation of pSi NPs was also seen in various organs such as the kidney, spleen and heart as well as in tumors (Figure 7). The remarkable increase in fluorescence intensity due to pSi NPs between the 4 and 24 h in tumors suggests a time-dependent build-up of pSi NPs. Such a build-up has been typically attributed to the "passive" accumulation of circulating NPs in solid tumors [5] through "leaky" vasculature, that is, via the interendothelial cell gaps (measuring up to 2000 nm) in tumor blood vessels, a phenomenon commonly referred to as enhanced permeability and retention (EPR). Recent work has suggested that rather than passive transport through interendothelial cell gaps as envisioned in EPR, the NPs enter solid tumors via active transport through *trans*-endothelial pathways [61]. In any case, the small NP size allows their accumulation in tumors [52].

The efficient accumulation of the LPep_pSi NPs in tumors at 4 h (Figure 7A) and further increase at 24 h (Figure 7B) suggest peptide–tumor biomarker/biomolecule interaction. Similar results have been reported in previous studies aimed at tumor targeting using functionalized pSi NPs (e.g., [18–20,62]). The presence only at the tumor region (and not in other organs) of LPep_pSi NPs at the 4th h suggests highly specific and efficient legumain binding by LPep_pSi NPs. The slightly higher amount of pSi NPs at the tumor relative to that of LPep_pSi NPs at the 24 h may point to the relative importance of particle size versus surface chemistry of the two types of NPs [52], an area that needs further elucidation [61].

Histopathological analysis confirmed that the method used to induce breast cancer in the mouse model was successful. Enlargement of the spleen was observed during the organ extraction, which is an indication of tumor induction in mice. There was no morphological change, damage or toxicity in the cerebellum, cerebrum, spleen, heart and stomach. The liver was normal in the nontumor groups and showed reactive changes such as congestion and inflammation that may be attributed to the secondary effects of the tumor metastasis. The kidneys showed congestion in the interstitium and casts in tubules, suggesting some mild damage due to the effects of pSi and LPep_pSi NPs, both of which cause some burden on the kidney at the dosage levels that were administered. The inflammatory changes in the lungs were nonspecific. Overall, the histopathological evaluation suggested that the experimented dosage for both pSi and LPep_pSi NPs at 20 mg/kg was ideal, as the toxicity signs observed were quite mild and insignificant. Previous studies using pSi and peptide-functionalized pSi NPs have also shown no signs of significant toxicity at a dose equivalent to or below 20 mg/kg [6,20,53,54].

Conclusion

Legumain-selective peptide-conjugated pSi NPs were produced for enhanced targeting and imaging of legumain-active cells. The legumain-targeting potential of two types of peptide, a linear 10-mer peptide and its branched (Y-shaped) equivalent, was investigated using *in vitro* experiments: qualitatively using confocal microscopy of cellular association in two cell lines with different legumain levels, namely RAW 264.7 and 4T1 and quantitatively with flow cytometry on four cell types with varying legumain activity, namely RAW 264.7, MCF 7, 4T1 and MCF 10A cells. The *in vitro* experimental results established that the linear peptide–pSi NPs have better aqueous stability under physiological conditions and higher legumain-binding efficiency toward legumain-expressing cells compared with those of the branched peptide–pSi NPs.

Subsequent *in vivo* studies (analyzed using *ex vivo* fluorescence of excised organs) with bare pSi NPs and linear peptide-conjugated pSi NPs on a syngeneic mouse model of breast cancer showed a higher accumulation of the peptide-conjugated pSi NPs in the tumor within 4 h of intravenous administration compared with that of nonconjugated pSi NPs. Cytotoxicity and histopathology data suggest that the biodegradable linear peptide-pSi NPs formulation is nontoxic, nonimmunogenic and suitable for drug-delivery applications. Although pSi NPs have

been widely studied for drug delivery and biosensing applications, to the best of our knowledge, this is the first study combining multifunctional and biocompatible pSi NPs with the emerging protease-targeting approach using legumain-specific peptides for drug-targeting applications. The linear peptide-pSi NP formulation is an efficient drug-delivery platform with potential for applications across a range of conditions (e.g., atherosclerosis, Alzheimer's disease and various cancers) where legumain plays a pathophysiological role.

Summary points

- Legumain plays significant roles in various diseases (e.g., cancers, atherosclerosis, multiple sclerosis, Alzheimer's disease, etc.) and its overexpression in tumor environments and narrow substrate specificity (cleavage after asparaginyl P1 site) allow the use of legumain-selective peptides to target the tumor microenvironment.
- A legumain-targeting, linear 10-mer peptide and its equivalent Y-shaped peptide-functionalized porous silicon (pSi) nanoparticles were synthesized using a microwave-assisted method.
- The zeta potential values and Fourier transform infrared spectral data confirmed the successful functionalization of the pSi nanoparticles with both (linear and Y-shaped) peptides.
- UV-visible light absorption and photoluminescence (PL) spectra of the pSi nanoparticles and functionalized peptide-pSi nanoparticles showed adequate light absorption in the UV-visible region and PL emission in the near-infrared region, suggesting their bioimaging potential.
- Stability studies indicated high aqueous stability for the pSi nanoparticles and linear peptide-pSi nanoparticles with varying pH, temperature, medium and time within ranges relevant to bioapplications. The Y-peptide-functionalized pSi nanoparticles were unstable at high temperatures.
- Flow cytometry studies revealed that the legumain-targeting efficiency of the different nanoparticle formulations was proportional to the legumain expression of the cell types.
- Quantitative flow cytometry data in conjunction with limited qualitative confocal microscopy data obtained using the nanoparticle formulation-treated cells showed the bioimaging potential of the peptide-pSi nanoformulations.
- *Ex vivo* biodistribution studies indicated rapid accumulation of the linear peptide-conjugated pSi nanoparticles in tumor tissue (within 4 h), suggesting the efficient targeting and bioimaging potential of the nanovector.
- Histopathological analysis confirmed the successful induction of breast cancer in a mouse model and validated the dosage of nanoparticles used (20 mg/kg) to be optimum.

Open access

Supplementary data

To view the supplementary data that accompany this paper please visit the journal website at: www.futuremedicine.com/doi/suppl/10.2217/nnm-2022-0017

Author contributions

Financial & competing interests disclosure

References

Papers of special note have been highlighted as: ● of interest

1. Ferrari M. Cancer nanotechnology: opportunities and challenges. *Nat. Rev. Cancer* 5(3), 161–171 (2005).

2. Gonzalez-Valdivieso J, Girotti A, Schneider J, Arias FJ. Advanced nanomedicine and cancer: challenges and opportunities in clinical translation. *Int. J. Pharm.* 599, 120438 (2021).

3. Canham LT. Silicon quantum wire array fabrication by electrochemical and chemical dissolution of wafers. *Appl. Phys. Lett.* 57(10), 1046–1048 (1990).

4. Canham LT. Bioactive silicon fabrication through nanoetching techniques. *Adv. Mater.* 7(12), 1033–1037 (1995).

5. Park JH, Gu L, Von Maltzahn G, Ruoslahti E, Bhatia SN, Sailor MJ. Biodegradable luminescent porous silicon nanoparticles for *in vivo* applications. *Nat. Mater.* 8(4), 331–336 (2009).

•   **An early detailed and influential study of intrinsically luminescent porous silicon (pSi) nanoparticles for nanotheranostics. The authors describe *in vitro* and *in vivo* biodistribution and time-dependent bioelimination of porous silicon nanoparticles. They demonstrate bioimaging and preliminary anticancer drug (doxorubicin) delivery and therapy using the pSi nanoplatform.**

6. Salonen J, Kaukonen AM, Hirvonen J, Lehto VP. Mesoporous silicon in drug delivery applications. *J. Pharm. Sci.* 97(2), 632–653 (2008).

7. Canham L. Introductory lecture: origins and applications of efficient visible photoluminescence from silicon-based nanostructures. *Faraday Disc.* 222, 10–81 (2020).

8. Stojanovic V, Cunin F, Durand JO, Garcia M, Gary-Bobo M. Potential of porous silicon nanoparticles as an emerging platform for cancer theranostics. *J. Mater. Chem. B* 4(44), 7050–7059 (2016).

•   **Excellent review of the theranostic potential of porous silicon nanoparticles with a focus on cancer treatment and diagnosis. Authors cover targeted anticancer drug delivery, photodynamic therapy and thermal therapies.**

9. Shen J, Kim HC, Su H *et al.* Cyclodextrin and polyethylenimine functionalized mesoporous silica nanoparticles for delivery of siRNA cancer therapeutics. *Theranostics* 4(5), 487–497 (2014).

10. Tzur-Balter A, Shtenberg G, Segal E. Porous silicon for cancer therapy: from fundamental research to the clinic. *Rev. Chem. Eng.* 31(3), 193–207 (2015).

11. Kumeria T, McInnes SJP, Maher S, Santos A. Porous silicon for drug delivery applications and theranostics: recent advances, critical review and perspectives. *Expert Opin. Drug Deliv.* 14(12), 1407–1422 (2017).

12. Park JH. Porous silicon for tumour targeting and imaging. In: *Porous Silicon for Biomedical Applications.* Santos HA (Ed.). Woodhead Publishing Limited, Cambridge, England, 403–419 (2014).

13. Park Y, Yoo J, Kang MH, Kwon W, Joo J. Photoluminescent and biodegradable porous silicon nanoparticles for biomedical imaging. *J. Mater. Chem. B* 7(41), 6271–6292 (2019).

14. Secret E, Smith K, Dubljevic V *et al.* Antibody-functionalized porous silicon nanoparticles for vectorization of hydrophobic drugs. *Adv. Healthcare Mater.* 2(5), 718–727 (2013).

15. Xia B, Zhang WY, Shi JS, Xiao S. Engineered stealth porous silicon nanoparticles via surface encapsulation of bovine serum albumin for prolonging blood circulation *in vivo*. *ACS Appl. Mater. Interfaces* 5(22), 11718–11724 (2013).

16. Britcher L, Barnes TJ, Griesser HJ, Prestidge CA. PEGylation of porous silicon using click chemistry. *Langmuir* 24(15), 7625–7627 (2008).

17. Godin B, Tasciotti E, Liu XW, Serda RE, Ferrari M. Multistage nanovectors: from concept to novel imaging contrast agents and therapeutics. *ACC Chem. Res.* 44(10), 979–989 (2011).

18. Kinnari PJ, Hyvönen MLK, Makila EM *et al.* Tumour homing peptide-functionalized porous silicon nanovectors for cancer therapy. *Biomaterials* 34(36), 9134–9141 (2013).

19. Secret E, Maynadier M, Gallud A *et al.* Two-photon excitation of porphyrin-functionalized porous silicon nanoparticles for photodynamic therapy. *Adv. Mater.* 26(45), 7643–7648 (2014).

20. Wang CF, Sarparanta MP, Mäkilä EM *et al.* Multifunctional porous silicon nanoparticles for cancer theranostics. *Biomaterials* 48, 108–118 (2015).

21. Kim D, Kang J, Wang T *et al.* Two-photon *in vivo* imaging with porous silicon nanoparticles. *Adv. Mater.* 29(39), 1703309 (2017).

22. Qi SC, Zhang PF, Ma M *et al.* Cellular internalization-induced aggregation of porous silicon nanoparticles for ultrasound imaging and protein-mediated protection of stem cells. *Small* 15(1), 1804332 (2019).

23. Spicer CD, Jumeaux C, Gupta B, Stevens MM. Peptide and protein nanoparticle conjugates: versatile platforms for biomedical applications. *Chem. Soc. Rev.* 47(10), 3574–3620 (2018).

•   **A comprehensive review of peptides and proteins as ligands for nanomedical applications. The authors discuss the advantages of using peptides (and proteins) in nanoconjugates for specific cell/tumor targeting and penetration.**

24. Chen G, Qian Y, Zhang H *et al.* Advances in cancer theranostics using organic–inorganic hybrid nanotechnology. *Appl. Mater. Today* 23, 101003 (2021).

25. Hou JT, Ko KP, Shi H *et al.* PLK1-Targeted fluorescent tumor imaging with high signal-to-background ratio. *ACS Sensors* 2(10), 1512–1516 (2017).

26. Ferreira MPA, Ranjan S, Correia AMR *et al*. *In vitro* and *in vivo* assessment of heart-homing porous silicon nanoparticles. *Biomaterials* 94, 93–104 (2016).

27. Kim YJ, Lee HI, Kim JK, Kim CH, Kim YJ. Peptide 18-4/chlorin e6-conjugated polyhedral oligomeric silsesquioxane nanoparticles for targeted photodynamic therapy of breast cancer. *Colloids Surf. B Biointerfaces* 189, 110829 (2020).

28. Dall E, Brandstretter H. Structure and function of legumain in health and disease. *Biochimie* 122, 126–150 (2016).

● **An authoritative review on legumain (asparaginyl endopeptidase). The authors discuss among others, the structure, occurrence, physiological and enzymatic functions, substrate specificity and pathological roles of legumain.**

29. Lunde NN, Gregersen I, Ueland T *et al*. Legumain is upregulated in acute cardiovascular events and associated with improved outcome–potentially related to anti-inflammatory effects on macrophages. *Atherosclerosis* 296, 74–82 (2020).

30. Liu C, Sun C, Huang H, Janda K, Edgington T. Overexpression of legumain in tumors is significant for invasion/metastasis and a candidate enzymatic target for prodrug therapy. *Cancer Res.* 63(11), 2957–2964 (2003).

31. Murthy RV, Arbman G, Gao J, Roodman GD, Sun XF. Legumain expression in relation to clinicopathologic and biological variables in colorectal cancer. *Clin. Cancer Res.* 11(6), 2293–2299 (2005).

32. Gawenda J, Traub F, Luck HJ, Kreipe H, Von Wasielewski R. Legumain expression as a prognostic factor in breast cancer patients. *Breast Cancer Res. Treat.* 102(1), 1–6 (2007).

33. Wang LN, Chen S, Zhang MN *et al*. Legumain: a biomarker for diagnosis and prognosis of human ovarian cancer. *J. Cell. Biochem.* 113(8), 2679–2686 (2012).

34. Ohno Y, Nakashima J, Izumi M, Ohori M, Hashimoto T, Tachibana M. Association of legumain expression pattern with prostate cancer invasiveness and aggressiveness. *World J. Urol.* 31(2), 359–364 (2013).

35. Li N, Liu QL, Su Q *et al*. Effects of legumain as a potential prognostic factor on gastric cancers. *Med. Oncol.* 30(3), 621 (2013).

36. Liu Y, Bajjuri KM, Liu C, Sinha SC. Targeting cell surface alpha(v)beta(3) integrin increases therapeutic efficacies of a legumain protease-activated auristatin prodrug. *Mol. Pharm.* 9(1), 168–175 (2012).

37. Smith R, Johansen HT, Nilsen H *et al*. Intra- and extracellular regulation of activity and processing of legumain by cystatin E/M. *Biochimie* 94(12), 2590–2599 (2012).

38. Edgington LE, Verdoes M, Bogyo M. Functional imaging of proteases: recent advances in the design and application of substrate-based and activity-based probes. *Curr. Opin. Chem. Biol.* 15(6), 798–805 (2011).

39. Yan L, Gao Y, Pierce R, Dai L, Kim J, Zhang M. Development of Y-shaped peptide for constructing nanoparticle systems targeting tumor-associated macrophages *in vitro* and *in vivo*. *Mater. Res. Exp.* 1(2), 025007 (2014).

40. Kanathasan JS, Gunasagaram D, Khan SU *et al*. Linear versus branched peptide with same amino acid sequence for legumain-targeting in macrophages: targeting efficiency and bioimaging potential. *ChemistrySelect* 5(32), 9911–9919 (2020).

41. Zhong YL, Peng F, Wei XP *et al*. Microwave-assisted synthesis of biofunctional and fluorescent silicon nanoparticles using proteins as hydrophilic ligands. *Angew Chem. Int. Ed. Engl.* 51(34), 8485–8489 (2012).

42. Bajjuri KM, Liu YA, Liu C, Sinha SC. The legumain protease-activated auristatin prodrugs suppress tumor growth and metastasis without toxicity. *ChemMedChem* 6(1), 54–59 (2011).

43. Amonkosolpan J, Wolverson D, Goller B *et al*. Porous silicon nanocrystals in a silica aerogel matrix. *Nanoscale Res. Lett.* 7, 397 (2012).

44. Sailor MJ. *Porous Silicon in Practice: Preparation, Characterization and Applications.* Wiley-VCH Verlag GmbH & Co. KGaA, Weinheim, Germany (2011).

45. Kong J, Yu S. Fourier transform infrared spectroscopic analysis of protein secondary structures protein FTIR data analysis and band assignment. *Acta Biochim. Biophys. Sin.* 39, 549–559 (2007).

46. Ji Y, Yang XL, Ji Z *et al*. DFT-calculated IR spectrum amide I, II, and III band contributions of N-methylacetamide fine components. *ACS Omega* 5(15), 8572–8578 (2020).

47. Xu YK, Adachi S. Multiple-peak structure in porous Si photoluminescence. *J. Appl. Phys.* 107(12), 123520 (2010).

48. Cheah KW, Chan T, Lee WL, Teng D, Zheng WH, Wang QM. Multiple peak photoluminescence of porous silicon. *Appl. Phys. Lett.* 63(25), 3464–3466 (1993).

49. Bimbo LM, Sarparanta M, Santos HA *et al*. Biocompatibility of thermally hydrocarbonized porous silicon nanoparticles and their biodistribution in rats. *ACS Nano* 4(6), 3023–3032 (2010).

50. Yakin FE, Barisik M, Sen T. Pore size and porosity dependent zeta potentials of mesoporous silica nanoparticles. *J. Phys. Chem. C* 124(36), 19579–19587 (2020).

51. Smith RL, Åstrand OAH, Nguyen LM *et al*. Synthesis of a novel legumain-cleavable colchicine prodrug with cell-specific toxicity. *Bioorg. Med. Chem.* 22(13), 3309–3315 (2014).

52. Blanco E, Shen H, Ferrari M. Principles of nanoparticle design for overcoming biological barriers to drug delivery. *Nat. Biotechnol.* 33(9), 941–951 (2015).

53. Anderson SHC, Elliott H, Wallis DJ, Canham LT, Powell JJ. Dissolution of different forms of partially porous silicon wafers under simulated physiological conditions. *Phys. Status Solidi.* 197(2), 331–335 (2003).

54. Sarparanta M, Bimbo LM, Rytkönen J *et al.* Intravenous delivery of hydrophobin-functionalized porous silicon nanoparticles: stability, plasma protein adsorption and biodistribution. *Mol. Pharm.* 9(3), 654–663 (2012).

55. Tanaka T, Mangala LS, Vivas-Mejia PE. Sustained small interfering RNA delivery by mesoporous silicon particles. *Cancer Res.* 70(9), 3687–3696 (2010).

56. Sarparanta M, Mäkilä E, Heikkilä T *et al.* ^{18}F-labeled modified porous silicon particles for investigation of drug delivery carrier distribution *in vivo* with positron emission tomography. *Mol. Pharm.* 8(5), 1799–1806 (2011).

57. Lu W, Xie ZY, Tang Y *et al.* Photoluminescent mesoporous silicon nanoparticles with siCCR2 improve the effects of mesenchymal stromal cell transplantation after acute myocardial infarction. *Theranostics* 5(10), 1068–1082 (2015).

58. Tzur-Balter A, Shatsberg Z, Beckerman M, Segal E, Artzi N. Mechanism of erosion of nanostructured porous silicon drug carriers in neoplastic tissues. *Nat. Commun.* 6, 6208 (2015).

59. Croissant JG, Fatieiev Y, Khashab NM. Degradability and clearance of silicon, organosilica, silsesquioxane, silica mixed oxide, and mesoporous silica nanoparticles. *Adv. Mater.* 29(9), 1604634 (2017).

•   **A timely and critical summary of the biodegradability and clearance of silicon and silica nanoparticles. The roles of particle size, morphology, pore size, porosity, surface functional groups, medium and so on are discussed.**

60. Souris JS, Lee CH, Cheng SH *et al.* Surface charge-mediated rapid hepatobiliary excretion of mesoporous silica nanoparticles. *Biomaterials* 31(21), 5564–5574 (2010).

61. Sindhwani S, Syed AM, Ngai J *et al.* The entry of nanoparticles into solid tumours. *Nat. Mater.* 19(5), 566–575 (2020).

62. Osminkina LA, Sivakov VA, Mysov GA *et al.* Nanoparticles prepared from porous silicon nanowires for bio-imaging and sonodynamic therapy. *Nanoscale Res. Lett.* 9, 463 (2014).